Impact of geometry on stretchable meandered interconnect uniaxial tensile extension fatigue reliability

M. Jablonski [a,*], R. Lucchini [b], F. Bossuyt [a], T. Vervust [a], J. Vanfleteren [a], J.W.C. De Vries [d], P. Vena [b,c], M. Gonzalez [e]

[a] Center for Microsystems Technology (CMST), Imec and Ghent University, Technology Park 914, B-9052 Gent-Zwijnaarde, Belgium
[b] LaBS, CMIC, Politecnico di Milano, Milan, Italy
[c] IRCCS, Istituto Ortopedico Galeazzi, Milano, Italy
[d] Philips Research, Philips Group Innovation, High Tech Campus 34/6.038, 5656AE Eindhoven, The Netherlands
[e] Imec, Kapeldreef 75, 3001 Leuven, Belgium

Received 18 June 2014
Received in revised form 12 September 2014
Accepted 12 September 2014
Available online 20 November 2014

1. Introduction

1.1. Goals

The general aim of this work is to equip system level engineers with a collective notion of the reliable interconnect geometries, as well as those geometries that are detrimental or hazardous and should be avoided, or carefully monitored in a complete stretchable system. In order to provide design rules we investigate the relation between geometry and lifetime in in-plane structured metal interconnects embedded in PDMS[1] encapsulation. This work builds upon the methods and findings reported in our previous publication [1] where more detailed background as well as DOE can be found. Fig. 1(a) represents the geometry of the interconnect in concern.

In a complete system the meandered interconnect connects stiff islands hosting electronic components. This layout grants significant deformation capability and electric functionality. The concept is illustrated in Fig. 1(b) and (c). More information on stretchable systems, example applications and references can be found in the work of Vanfleteren et al. [2].

We study the effect of the meander geometry and that of the encapsulation on the time to the electro-mechanical failure of the interconnect in cyclic stretching tests. Furthermore, finite element analyses are used to explain the observations made through Weibull lifetime analysis, as well as to perform parametric sweep past the capabilities of an experiment.

1.2. Background

We are particularly interested in the structured metal interconnect of meandered shape due to the large area, conformable circuit applications in mind, which translates into the following requirements:

- Very high conductivity (generally above 10^5 S/cm, for efficient, large area, mid power circuits, e.g. light engines).

* Corresponding author. Tel.: +32 92645369.
E-mail address: michal.jablonski@elis.ugent.be (M. Jablonski).

[1] Polydimethylsiloxane

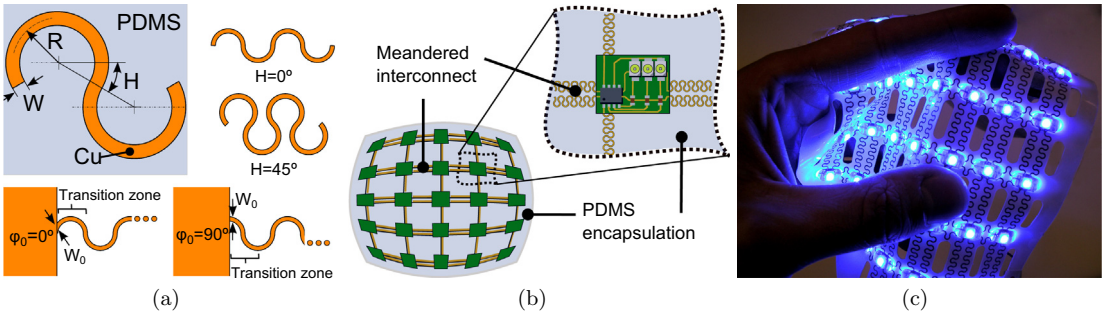

Fig. 1. (a) Meander definition and its geometry parameters. (b) Stretchable interconnect utility in a conformable system. (c) Example stretchable light engine system.

- Ease of development using standard electronics manufacturing processes and equipments (transfer to industry).
- Electrical stability under strain (no significant resistance-strain dependence and no significant resistance-wear dependence).

Reviewing the stretchable technologies developed in the recent years [3–10] we find no stretchable, conductive, composite elastomers that fulfill these requirements all at once. Only structured metals (meanders [11–14], meshes [15], yarns or buckled films [16]), forming a stretchable interconnect exhibit electro-mechanical properties that can fulfill the above mentioned requirements. In particular, in-plane meandered interconnect (Fig. 1(a)), studied in this work, even if one penalizes bulk copper conductivity of $\approx 6 * 10^5$ [S/cm] proportionally to the added current path due to meandering, delivers, what one could define as equivalent conductivity of $2.5 * 10^5$ [S/cm], for a typical geometry of $H = 30°$. Approximately, this holds for any R since the running length of the meander can be shown to be independent of radius. This conductivity is still about 31 times higher than the silver nanowires based, elastomer composite solution developed by Xu and Zhu [10] – the most conductive, stretchable composite known to authors that allows resistance stability under mechanical load.

2. Materials and methods

2.1. Test vehicle

Fig. 2(a) represents a single test vehicle realized in 17 μm thick copper (Circuit Foil BF-HF-LP2) by means of photolithography, using dry film photoresist (DuPont Riston FX 920) and wet copper etching. The processing is carried out on a sacrificial FR4 carrier. The carrier is removed after embedding the top of the structured copper by 0.5 mm thick PDMS (Dow Corning, Sylgard 186), by means of liquid injection molding. Finally, the opposite side of the copper structure is encapsulated by injection molding. A detailed SMI processing is illustrated in another publication of our group [2]. The test vehicle can be divided into two functional zone types, the flexible only zones, realized by the large copper spill areas (bright areas in Fig. 2(a)) and two flexible, but also stretchable zones, containing the stretchable interconnects (transparent areas appearing darker in Fig. 2(a)). The two stretchable zones are bridged by meandered interconnects, a pair of each connected electrically in series (please refer to Appendix B (Fig. 15) for test vehicle dimensions and indication of test current paths).

2.2. Endurance test

The test vehicle, shown in Fig. 2(a), is fixed in the test setup and connected to the resistance measurement system (please see Appendix A). The reading in Fig. 2(b) is obtained by means of 4 point resistance measurement while the test vehicle undergoes repeated tensile elongation using an Universal Testing Machine (UTM). Fig. 2(b) illustrates the high electrical stability and low resistance delivered by a series chain of two, 1 cm long, copper interconnects, registered under repeated, 10% interconnect strain-a generic endurance output in this reliability study. Please note the logarithmic scale on the vertical axis. Some spread of the instantaneous reading was present due to a random noise pickup during

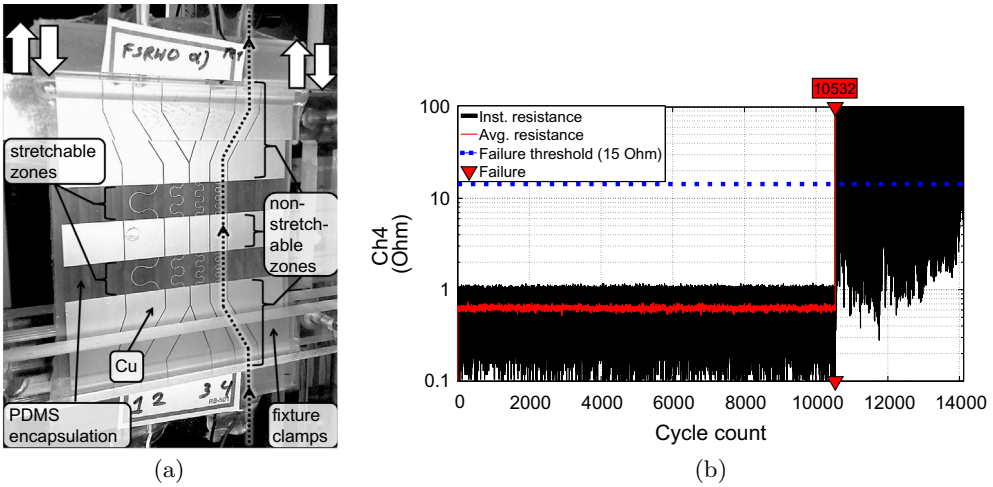

Fig. 2. (a) Test vehicle fixed in the UTM. Dotted line indicates test current path for the resistance measurement in the 4th meander chain. (b) Meandered interconnect resistance reading taken during the 10% uniaxial stretching endurance test.

UTM actuation, not an actual change of meander resistance, therefore an averaged reading is also provided.

The moment of mechanical failure of the copper track due to fatigue is equivalent to an abrupt electrical failure (Fig. 2(b)) and is registered in function of performed stretching cycles. The same stable behavior and sudden failure was also reported previously by de Vries et al. [17]. A number of failures observed produces a statistical sample of times to failure, based on which, the underlying failure distribution is modeled using a two parameter Weibull CDF (Cumulative Distribution Function). We use this particular model because of its historically proven applicability in reliability modeling of metals, as well as due to the structure of the meandered interconnect, the failure of which can be viewed as a failure of the weakest chain link. Similar analysis on a family of meandered interconnect technologies has been previously performed by de Vries et al. [17].

3. Theory/calculation

3.1. Statistical tools

The underlying Weibull distribution parameters[2] were found using a simple Median Rank Regression (MRR) method in case of vehicles carrying 4 different radius (R) meanders (here referred to as geometry FSRW-Flex-Stretch-Radius-Width), and using Maxi-mum Likelihood (ML) method in case of vehicles carrying 4 identical meanders (geometry FSTR- Flex-Stretch-Transition). Please consult Appendix B (Tables 2–4) for interconnect geometries and nomenclature. The use of MRR was dictated by only one failure per meander type obtained in each run by virtue of FSRW vehicles design. The rationale behind this design was to be able to fit a set of meanders spanning wide in R parameter in a relatively small space available on the test sample while ensuring each meander was far away from the encapsulation boundaries. More detail on DOE is explained in our previous publication [1]. As a consequence we could obtain only one failure per meander type, per fatigue run, which increased the amount of vehicles needed to obtain sufficient failure points as well as introduced some variability between each run execution (e.g. slight changes in test vehicle fixing or starting point for the tensile extension which can be expected to introduce fuzziness in the failure data). The combination of limited sample size and underlying experimental variability were considered as volatile conditions for use of ML estimate [19], hence the conservative MRR method is preferred. The MRR fitting method was executed using a custom MATLAB script. The remaining vehicles of type FSTR had 4 identical meanders each, producing sufficient amount of failures using as little as two to three test vehicles (two/three UTM runs). This enabled the use of ML method which adds robustness against outliers to the inference of the underlying model as well as enables the calculation of the Weibull parameter confidence intervals. The ML estimates of the two distribution parameters, β (shape) and η (scale), were found by MATLABs Statistics Toolbox function wblfit() that computes the solution to the Weibull Maximum Likelihood function maximization problem. Interested reader can find out more about the Maximum Likelihood method in [20] as well as its application for Weibull distribution in [21]. Moreover, a critical comparison of the two inference methods used in this work is provided by Genschel and Meeker [22].

[2]
$$f(N) = \frac{\beta}{\eta}\left(\frac{N}{\eta}\right)^{\beta-1} \exp\left[-\left(\frac{N}{\eta}\right)^{\beta}\right] - \text{Weibull PDF}$$

$$F(N) = 1 - \exp\left[-\left(\frac{N}{\eta}\right)^{\beta}\right] - \text{Weibull CDF}$$

where N – number of fatigue cycles, η – scale parameter (characteristic life), β – shape parameter [18].

3.2. Test vehicle selection, result suspension and censoring

Before each run the vehicles were inspected using a microscope and a multimeter. Sporadically, vehicles had inadequate definition of meanders or meanders with an electrical failure due to a photolithography fault. These faulty meanders were discarded from analysis. As a result some small size differences between samples were allowed. The pre-selection was done to ensure that the samples are representative and differ due to defined geometries and not due to external factors related to production yield. No censoring was used in all the new results presented (all failures occurred before the end of the test) with one exception, where an accelerated failure generated by an etching fault; that had passed the initial inspection unnoticed, has been suspended (vehicle FSTR0 HE, suspension at 7798 cycles).

The same failure mode was identified for all remaining data. Metal track was ruptured due to rapid crack buildup in the zones of highest plastic strain concentration which corresponds to the rapid electrical failure as illustrated by the reading in Fig. 2(b).

3.3. Modeling tools

The computational models were realized using the commercial finite element code Abaqus/Standard (Dassault, Systemes Corp., RI, USA). Since the symmetry of the problem allows for reduction of the region of interest, only half of the sample was modeled, reducing the analysis to a single row of meanders. Symmetry boundary conditions were applied on one side of interconnects, while on the other side a 10% of stretch was applied through displacements conditions to reproduce the experimental configuration, considering the flexible part connected to the clamp as rigid. Mesh sensitivity analyses allowed to estimate an optimal mesh density for the global models in the range $3 * 10^5$–$4 * 10^5$ linear hexahedral elements, in order to have at least four elements across the width of the meander track, enough to provide accurate results. The copper was modeled as a perfect elasto-plastic material by the Von Mises yield criterion, with the elastic Young's module $E = 117$ GPa and the yielding point at $\sigma_y = 0.370$ GPa. A Neo-Hookean strain energy function, $C10 = 0.157$, was selected to represent the hyperelastic behavior of the PDMS. PDMS was considered incompressible. In order to avoid intrinsic computational ill conditioning of incompressible materials, hybrid elements have been used to simulate the PDMS mechanical response. The accumulated plastic strain per cycle was considered as representative for the critical regions where the metal cracking initiates and, eventually, rupture occurs. A number of four stretching cycles were applied in order to reach a steady state condition past which the accumulated plastic strain per cycle is constant [23,24].

4. Results

4.1. Metal geometry impact on reliability

4.1.1. Radius effect

In our previous work [1] we have found frequent zero-hour failures and infant mortality in a large, R = 2.9 mm copper meanders. Smaller meanders, instead, exhibited much better cyclic performances evaluated in the same fatigue conditions. In the current work, a FEM model replicating the geometry of the stretchable zone of that test vehicle (geometry FSRW0) was prepared as shown in Fig. 3(a).

Comparison of the FEM results in Fig. 3(b) across different radii meanders confirms a severe plastic strain localization in the large meander track. The region of the high plastic strain overlaps well with the location of the zero-hour and early failures found in the

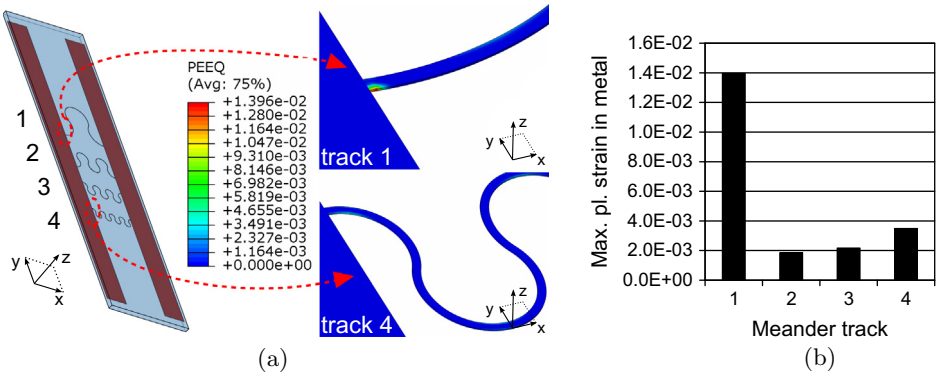

Fig. 3. FEM modeling result – maximum, equivalent plastic strain accumulated in the 4th cycle to 10% interconnect elongation. (a) FEM model and maximum plastic strain regions in track 1 and 4. (b) Comparison between all meanders.

previous experiment [1]. Further finite element analyses addressing different encapsulation thickness (Section 4.2.1) will provide a mechanical interpretation of the above result.

4.1.2. Effect of meander rotation

In [1] it was also shown that the amount of metal in the interconnects affects the failure distribution parameter β, thus highlighting the relevance of metal distribution. One way to achieve a straightforward visualization of the interconnect metal distribution is to simply project the metal length onto an axis perpendicular to the tensile force direction. One can use a simple algorithm integrating column-wise on a high resolution bitmap image of the interconnect to realize such a distribution profile. Fig. 4(a) represents the simple interconnect FSRW0 and a profile obtained by this method.

Knowing that adding metal was not the way to proceed toward higher reliability we were interested to see how the interconnect would respond to a significant metal redistribution, and if that could bring reliability improvement. One way to redistribute the metal without adding more copper to the interconnect or changing the parameters of the meanders is to rotate it with respect to the tensile force direction. A vehicle FSRW0 Fi5 was prepared, where all the meanders were rotated by 5° compared to the baseline geometry FSRW0. Fig. 4(b) illustrates the rotated interconnect and its metal distribution.

Fig. 4(c) and (d) compare the reliability result from the 10% strain endurance tests performed on the two vehicles. The largest meander is not visible in both the Weibull charts because it was being damaged already during vehicle preparation due to its sensitivity to plastic strain concentration as presented in the simulation

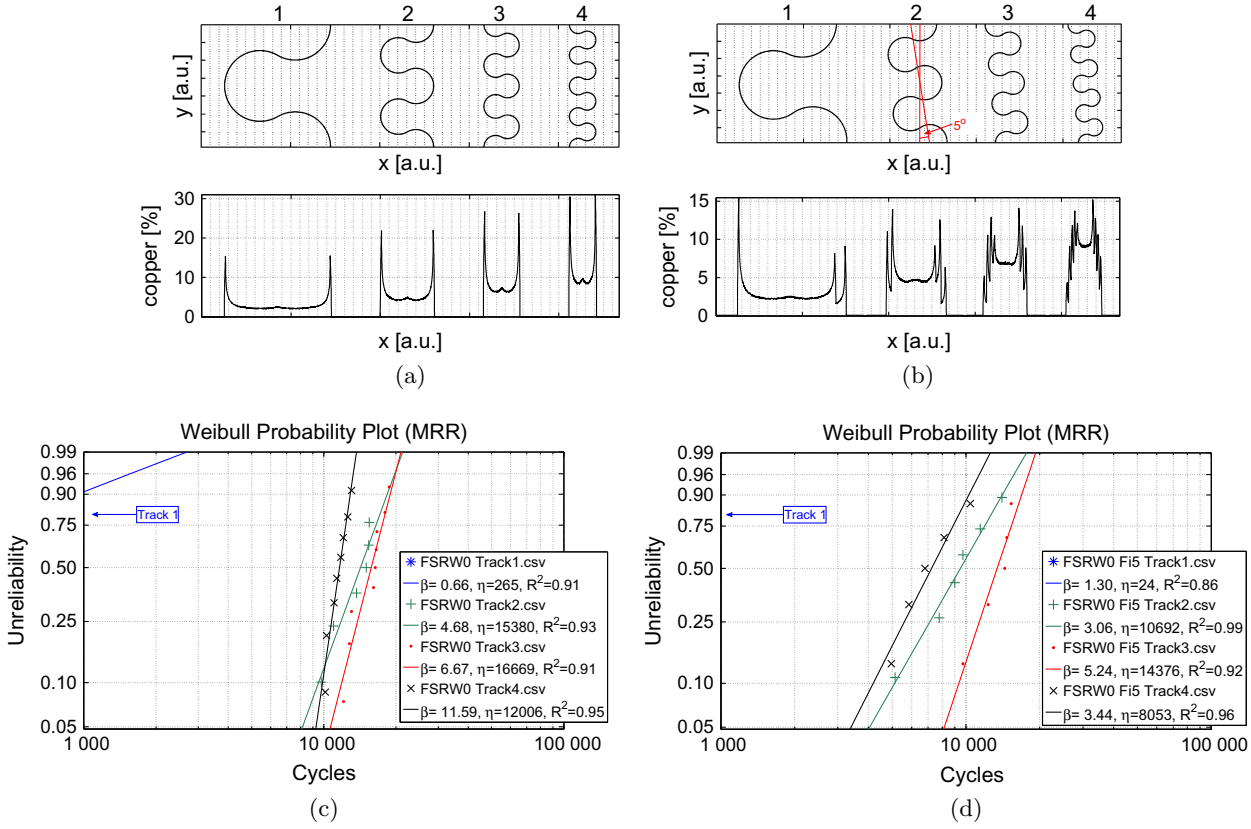

Fig. 4. (a and b) FSRW test vehicle geometries (top) and their copper distribution (bottom). (c and d) corresponding Weibull plot and failure models for 10% elongation, uniaxial tensile fatigue life per meander type.

results in Section 4.1.1. In the remaining, fatigue failures obtained in tracks 2,3, and 4 the failures occur more randomly (lower β, as expected) in rotated meanders compared to the 'straight' ones as visible by comparing all results in Fig. 4(c) and (d). Along with the shape parameter however, also the characteristic life is diminished in all rotated tracks, leading to an overall decrease in reliability of the rotated meanders.

4.1.3. Transition geometry effect

Another transition geometry was evaluated which is illustrated in Fig. 5. This particular transition design is very attractive since, unlike the previous attempt at meander transition reinforcement [1] and the simple transition FSTR0, it has a scalable geometry (Fig. 5), that does not introduce any additional parameters to the meander definition.

Please note how this modified transition does not increase the peak interconnect copper distribution values, but instead redistributes the material in Fig. 6 compared to the simple transition.

Both geometries FSTR0 (simple transition) and FSTR1 (tapered transition) were compared in a 10% uniaxial tensile strain fatigue test. Both geometries had approximately the same meander radius $R \approx 1$ mm (exact parameters can be found in Appendix B). The reliability result is presented in Fig. 6 and indicates that the tapered transition is largely under-performing, producing some 50 times shorter characteristic life compared to the simple design. All failures in tapered meanders were found in transition only whereas in the FSTR0 vehicle the failures in the transition parts and in the middle of the interconnects were approximatively equally distributed, being 44% and 56%, respectively.

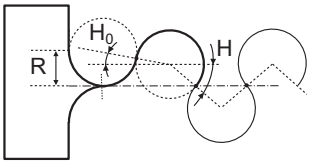

Fig. 5. FSTR1, tapered geometry transition rule, where H_0 is uniquely defined for a given $H : H_0 = (1 - \sin(H))/2$.

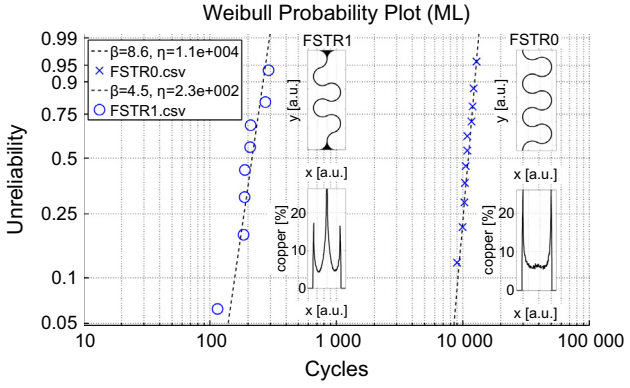

Fig. 6. Comparison of 10% tensile strain fatigue life between a simple (FSTR0) and tapered interconnect (FSTR1). Next to the failure models are the metal geometries (top) and their corresponding copper distributions (bottom).

FEM of the tapered transition meander ($R = 0.91$ mm) revealed 40 times higher maximum plastic strain accumulated in the 4th cycle of elongation compared to the simple transition meander of the nearest radius ($r = 0.96$ mm). Fig. 7 compares the plastic strain distributions in both interconnects. In simple meander the plastic strain is evenly distributed between all meander heads, while in tapered design the plastic strain concentrates in the transition zones. This is in agreement with the spatial failure locations found in the two interconnects by experiment.

4.2. Encapsulation parameters impact on reliability

4.2.1. Encapsulation thickness effect

FEM model, including the different radii meanders (geometry FSRW0) was evaluated with varying thickness of encapsulation as indicated in Fig. 8(a), keeping the metal layer in the middle of the encapsulation thickness (t), in each case. The maximal plastic strain accumulated in metal, after 4 cycles of 10% axial strain, was extracted. The results across each meander in combination with each encapsulation thickness are presented in Fig. 8(b).

The large meander shows very high sensitivity to encapsulation thickness t. Up to 0.4 mm thickness the models indicate there is no plastic strain in meander 1 (elastic region is never exceeded), above that thickness the plastic strain accumulation in track 1 exceeds that of meanders 2, 3 and 4, reaching about 5 times higher plastic strain with 1 mm encapsulation, compared to the remaining meanders. Results obtained for track 1, 2 and 3 show steadily decreasing plastic strain with decreasing encapsulation thickness and generally align with those of Hsu et al. [25].

We were able to confirm the decreasing plastic strain concentration in meanders with decreasing encapsulation thickness by obtaining an improved lifetime in a 10% strain, fatigue test on a simple reliability vehicle FSTR0. The vehicle was built in two variants with full, $t = 1$ mm encapsulation and in half-encapsulated version (FSTR0 HE), where the meanders were covered only on one side with 0.5 mm encapsulation. A schematic of the cross sections of both vehicles can be found in Fig. 9(a), along with the Weibull reliability plot from the failure data. Improved reliability can be seen in the half-encapsulated vehicle. Fig. 9(b) confirms the significance in characteristic life change due to encapsulation

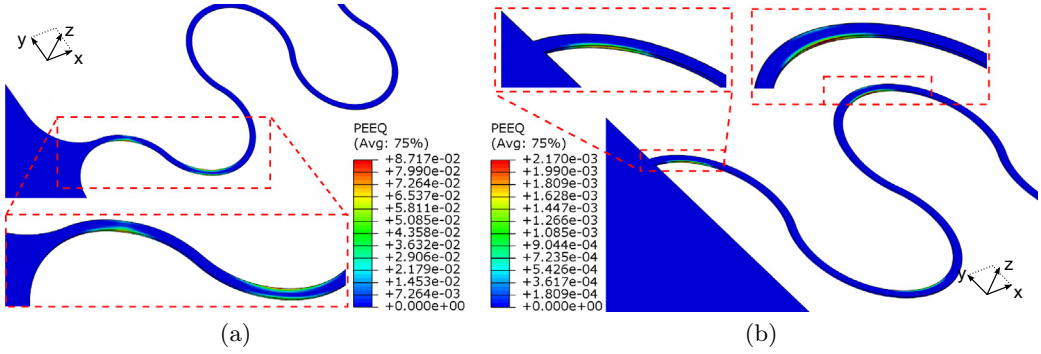

Fig. 7. Equivalent plastic strain in metal after the 4th cycle of 10% interconnect elongation. (a) Tapered design (FSTR1), $R = 0.91$ mm. (b) Simple design (FRTR0), $R = 0.96$ mm. Please note that the encapsulation around the metal has been removed from the view.

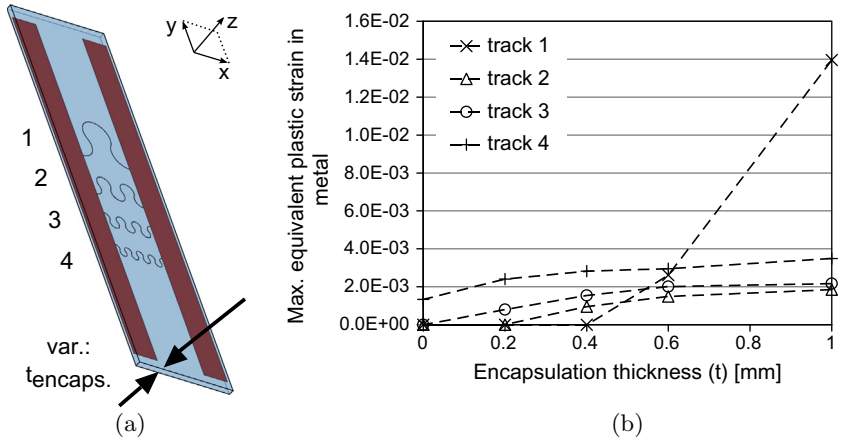

Fig. 8. (a) FEM model of the FSRW0 meander geometry realized in 5 variants of differing encapsulation thickness (t). (b) FEM result – maximum equivalent plastic strain per meander track accumulated in the 4th cycle of 10% interconnect extension.

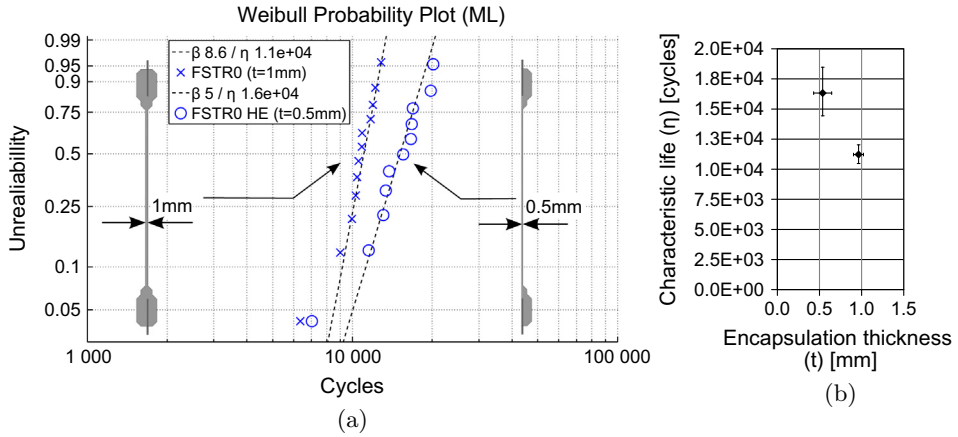

Fig. 9. (a) Reliability comparison between the full ($t \approx 1$ mm), and half-encapsulated meanders ($t \approx 0.5$ mm). (b) Weibull characteristic life parameter estimated by the ML method. The vertical error bars indicate 95% confidence interval for parameter η. The horizontal bars indicate 2SD of the test vehicles thickness.

thickness. Horizontal bars in Fig. 9(b) indicate 2SD encapsulation thickness spread between vehicles due to liquid injection molding process tolerance. The thickness was measured over the stretchable zone using soft materials thickness gauge MTG from Checkline, supplied with 16 mm footer with 212 g mass.

4.2.2. Encapsulation perimeter effect

In this experiment we evaluated the impact of lateral deformation of meanders due to a Poisson effect in the encapsulation, which was earlier reported in simulation results by Gonzalez et al. [26].

FSTR0, simple meander geometry vehicles were prepared, differing in the width of the specimen while keeping constant the interspace between adjacent meanders, Fig. 10(a), (d) and (g). The base test vehicle geometry had a 73 mm wide interconnect while, by removing parts of base encapsulation by sharp scalpel, the encapsulation in the remaining vehicles was reduced to 52 mm and 36 mm width respectively. By changing the aspect ratio of the stretchable zone we could expect different level of lateral compression in interconnects under the same tensile strain.

Each vehicle type was evaluated for reliability under repeated, 10% uniaxial strain conditions. The corresponding results of Weibull analysis are presented in Fig. 10(b), (e) and (h). In the case of the narrow encapsulation vehicle (Fig. 10(h)) the reliability results could not be properly fitted with a Weibull distribution. By tracing back each failure with its position in the vehicle the outer tracks (nr. 1 and 4) and the inner tracks (nr. 2 and 3) were found belonging to a distinct failure model each. Following, the data was divided into two separate clusters, giving approximate ML distribution fit for inner and outer tracks separately, as visible in Fig. 10(i). The outer tracks are indicated as less reliable than the inner ones. The clustering procedure for inner and outer tracks was repeated for the remaining vehicles with 52 mm and 73 mm wide encapsulation. The corresponding results are visible in Fig. 10(f) and (c). By comparing all three clustered results, the gradual decrease of reliability can be followed in the outer tracks as the PDMS boundary moves closer to the outer meanders. Please note that the high variability of β in the fitted distributions should be assigned to the very small statistical samples remaining after clustering.

4.2.3. Encapsulation hardness effect

A number of FSTR0, simple meander geometry vehicles were prepared, with differing PDMS encapsulation hardness. Different silicones from Dow Corning were used- see Table 1. The aim was to asses the impact on reliability due to the encapsulation hardness in the lower Shore-A range. We use hardness measure due to its widespread use in silicone products datasheet).

After mixing the two components for three minutes, a 5 min vacuum chamber degassing was performed; afterwards, liquid injection molding and curing in oven at 50 °C for 24 h was carried out. Table 1 lists the silicones and apparent Shore A hardness

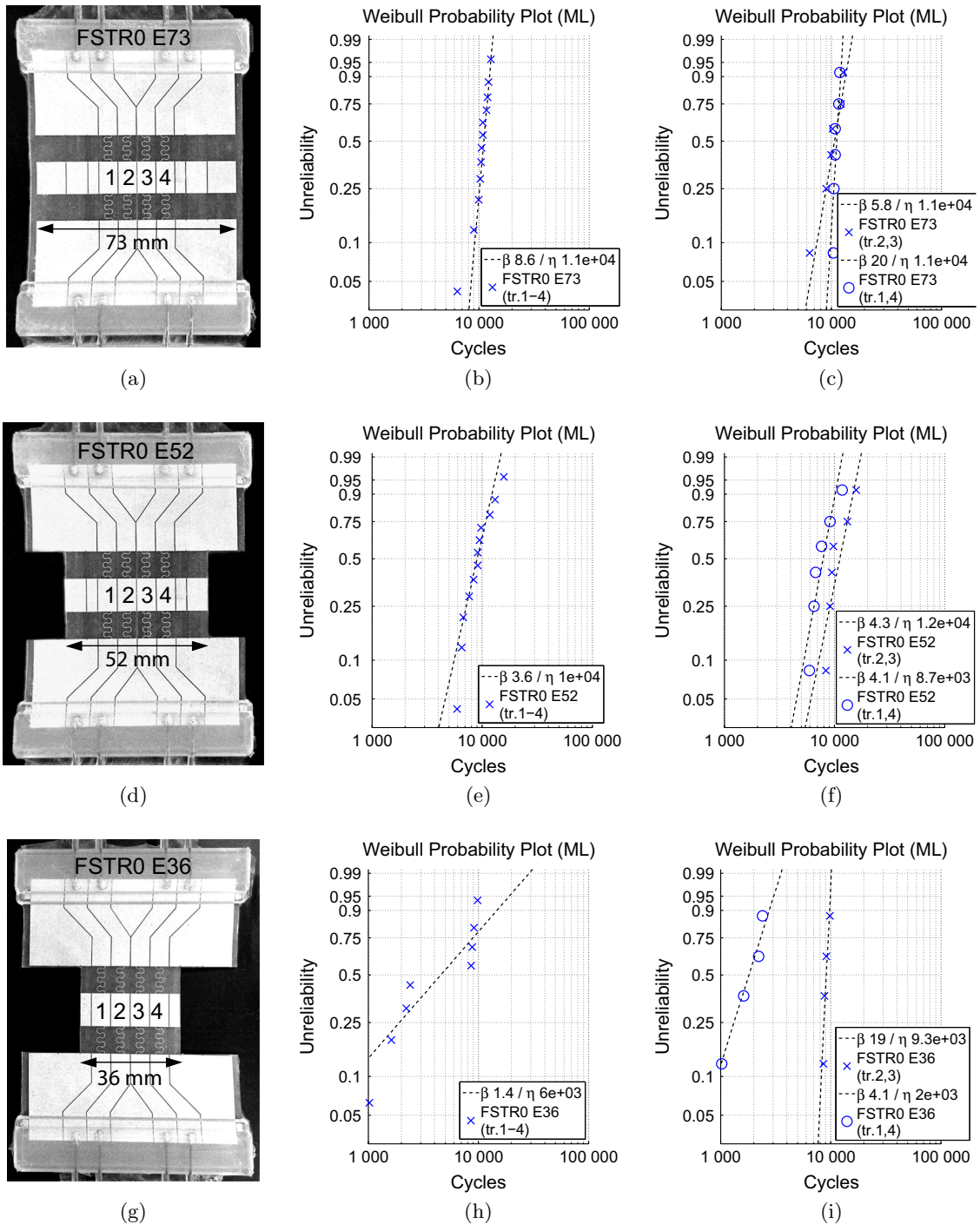

Fig. 10. Left column (a,d,g) – FSTR0 test vehicles in modified encapsulation perimeter variants. Middle column (b,e,h) – Weibull reliabilities in 10% tensile strain test obtained with fatigue testing of the corresponding vehicles. Right column (c,f,i) – Reliability analysis repeated after clustering the failures between inner tracks (2, 3) and outer tracks (1, 4).

obtained in each test vehicle as a result. The hardness was measured using a Checkline Durometer type RX-DD-A at the ends of each specimen where the PDMS was the thickest (9 mm) providing a 10 × 80 mm perimeter of solid material for the hardness test. It should be noted that the MS1003 material was not completely crosslinked after the 50°C cure, leading to hardness much below that indicated by the material datasheet (28 vs. 51 Shore A). The recommended curing temperatures for MS1003 are in excess of 100 °C, not applicable in our case due to the limitation of the PMMA mold used for the realization of the reliability test vehicles

Table 1
Shore A hardness of the encapsulation based on material type. Please note that the low hardness of MS1003 resulted from curing temperature limitation of 50 °C.

Encapsulation	Apparent hardness
Sylgard 184	45.6 (1SD)
Silastic E	36.6 (1.8SD)
Sylgard 186	35.0 (0.6SD)
MS1003	28.5 (0.9SD)

Table 2
FSRW0 test vehicles meander parameters. Left- Base geometry, Right-rotated geometry (each meander rotated 5° off vertical axis.

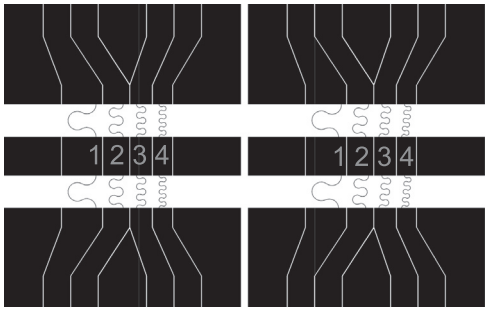

Track	$R[mm]$	$W[\mu m]$	$H[^o]$	$\phi_0[^o]$	W_0
1	2.89	100	30	90^o	W
2	1.44	100	30	90^o	W
3	0.96	100	30	90^o	W
4	0.72	100	30	90^o	W

Table 3
FSTR0 test vehicles meander parameters.

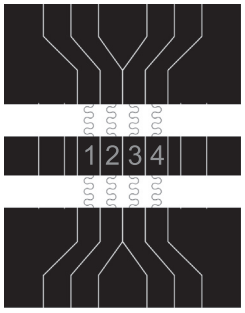

Track	$R[mm]$	$W[\mu m]$	$H[^o]$	$\phi_0[^o]$	W_0
1-4	0.96	100	30	90^o	W

Table 4
FSTR1 test vehicle meander parameters.

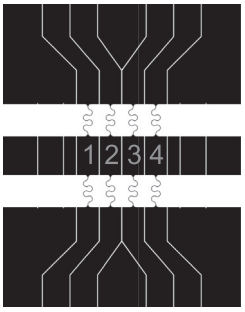

Track	$R[mm]$	$W[\mu m]$	$H[^o]$	ϕ_0 , W_0
1-4	0.91	100	30	see Fig.5

[1]. Additionally, because the Silastic E and Sylgard 186 materials provided very similar levels of hardness, the failure samples generated from both silicone types were merged into a single, Shore A36 statistical sample. The result of the fatigue test to 10% strain can be found in Fig. 11(a). The failure locations are very similar in all vehicles leading to no significant differences in reliabilities, as illustrated by Fig. 11(b).

5. Discussion

In this section we discuss the presented results and attempt to explain the observations as well as indicate importance of a given parameter effect for reliability.

5.1. Metal geometry effects

FEM result in Section 4.1.1 confirms our earlier, empirical findings by indicating very high sensitivity of the large, *R* = 2.9 mm meander to tensile elongation [1]. The sensitivity exhibited itself as about 5 times higher plastic strain accumulation in the 4th, simulated cycle of stretching to 10% strain, compared to the remaining, smaller meanders. In the empirical study this sensitivity led to damage already during processing (sample release from the mold) producing zero-hour failures or high failure variability in the reliability analysis as indicated by low Weibull shape parameter $\beta <$ 2 in Fig. 4(c). This effect was reproducible in meanders of the same size in a reliability test that followed, as shown in Fig. 4(d).

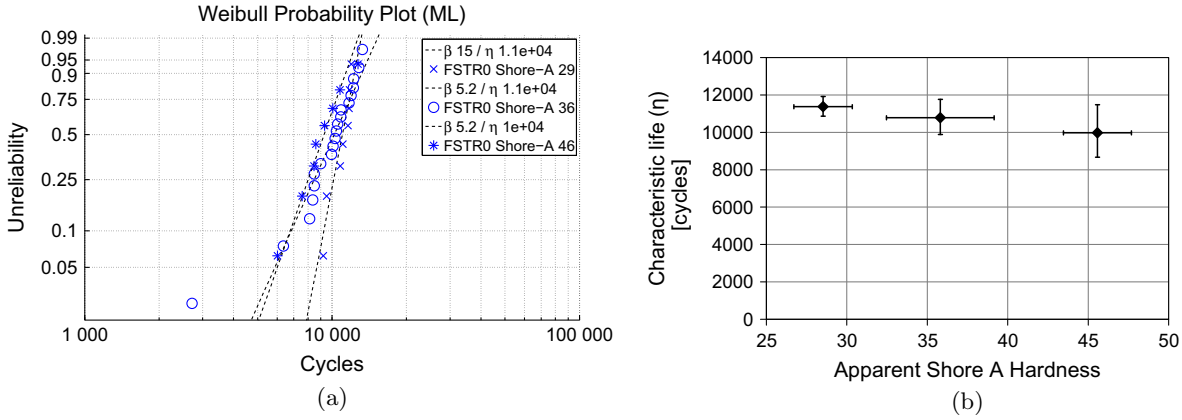

Fig. 11. (a) Weibull analysis of failures obtained with FSTR0 geometries in a 10% tensile strain fatigue test. Vehicles differed in hardness of encapsulation. (b) ML estimate of the characteristic life of interconnects in function of encapsulation hardness. The vertical error bars indicate 95% confidence intervals for the characteristic life parameter. The horizontal error bars indicate 2 × SD of the hardness measurement.

From beam theory it should follow that a large curvature meander should accommodate deformation (meander opening) with the lowest stresses in its structure compared to small curvature features. Moreover the large meander introduces the least amount of copper into the interconnect (see Fig. 4(a)). The failure data and the modeling results we collected however, pointed in the opposite direction. In order to explain the discrepancy between the theory and our results we analyze the encapsulation thickness effect further on in Section 5.2.

Reliability results in Section 4.1.2, track 2, 3, 4 indicate that meander rotation has a detrimental effect on reliability regardless of meander radius *R*. By applying a 5° rotation to the meanders the randomness of failure in all tracks has increased compared to the base configuration. This observation is in agreement with the claim made in our previous publication that the amount of copper introduced by the meandered interconnect is related with the Weibull shape parameter of the failure distribution [1].This is visible by comparing the steepness of the failure data fits and the metal distribution profiles in Fig. 4. The significance of this result is, that in stretchable electronic systems, meanders misaligned with the assumed direction of tensile forces will produce larger variability and increase chance of failure at low cycles compared to meanders aligned with the tensile force direction. This should be avoided by design or otherwise accounted for in estimation of the worst-case, low tail system reliability, significant for attaching warranties to product lifetimes.

Reliability results in Section 4.1.3 show the sensitivity of the interconnect to the metal geometry at the transition. In this result, as well as our previous study [1], we show that the simple transition with phase $\phi_0 = 90°$, and with no tapering at the transition zone is much more reliable than the tapered transitions. On one hand, the tapered meander end may be causing more stiffness in transition, which results in a lower stretchability of the interconnect that, additionally, is made effectively shorter by the tapered parts. On the other hand, the resilience of the simple geometry may be coming from the way in which the first meander head cou-ples with the non-stretchable region, restraining deformation of metal in the transition zone. This effect does not exist in the scal-able design FSTR1 because the presence of the tapered part at meander end offsets the distance between the non-stretchable border and the first meander head.

5.2. Encapsulation geometry effects

FEM presented in Section 4.2.1 evaluated performance of the interconnects of varying radii under varying encapsulation thickness. The plastic strain accumulation presented in Fig. 8(b) indicates strong coupling effect between the largest radius meander and the encapsulation thickness. Note that the same meander, track 1, $R = 2.9$ mm, which exhibits about 5 times higher plastic strain accumulation than the remaining tracks 2, 3 and 4 at 1 mm encapsulation, is the best performer below 0.5 mm encapsulation.

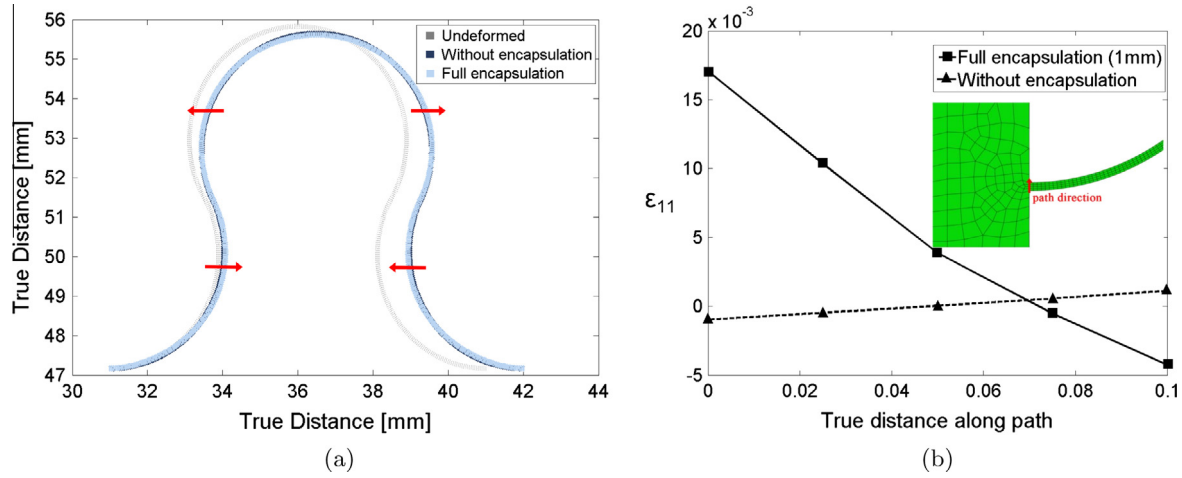

Fig. 12. (a) In-plane deformation difference between encapsulated and non-encapsulated meander. (b) Comparison of strain distribution between encapsulated and non-encapsulated meander in transition zone.

This combination of results indicates that a different metal deformation mechanism occurs at different encapsulation thickness. One should also consider the high Poisson ratio of PDMS ($\nu \approx 0.5$). Upon tensile extension of the interconnect in direction x, the encapsulation contracts in both remaining y and z direction to maintain volume. The compressive strain components contrib-ute to achieve a different deformation of the meander depending on the presence of encapsulation. The FEM results have shown that, at the end of the last loading cycle the meander without PDMS encapsulation exhibits a lower curvature at the attachment to the flexible area, compared to the model with encapsulation (Fig. 12(a)). The high thickness of PDMS used for encapsulation enforces the meander deformation due to PDMS contraction in the direction perpendicular to the loading direction resulting in an increased strain gradient along the cross section of the copper. This eventually leads to higher plastic strain accumulated over the loading cycles for encapsulated models, Fig. 12(b). In case of smaller meanders the presence of the track in the elastomer has a locally restricting effect on PDMS tensile extension at the meander heads, which results in less transverse encapsulation compression in these regions, as show in the work of Hsu et al. [25], which may explain the differences depending on R, observed in our study.

Results obtained for track 1, 2 and 3 generally align with those of Hsu et al. [25] showing steadily decreasing plastic strain with decreasing encapsulation thickness. These results agree also with those of Gonzalez et al. [27] who points out that higher aspect ratio (R/W) meanders attract lower plastic strain. As presented in our results, this rule applies up to a certain, maximal R/W, past which the exact opposite effect is observed (the larger meander, the higher plastic strain).

We now know, that thick encapsulations will encourage this effect. In combination with the Weibull shape parameter increasing with decreasing R [1] one should be considering larger meander designs more hazardous because high R interconnects will develop higher chance of early failure. This effect will be pronounced in circuits comprised of many interconnects by affecting the characteristic life of a system (please consider the series system unreliability Eq. (1) for high k and low β which is introduced further). One should take into account that these conclusions hold for fatigue life at moderate interconnect extension and may not be optimal for larger strains or one time stretchability to failure (e.g. choosing for small R will probably encourage earlier PDMS/metal delamination failure described by Hsu et al. [25] at high interconnect elongations simply because small R interconnect introduces more metal into the stretchable zone (Fig. 4(a)).

The result presented in Fig. 8(b) is not only significant for suitable selection of meander parameters, but also a guide for proper stretchable interconnect simulation. With these results we show that by neglecting the presence of even very thin and soft encapsulation in FEM the real over-encapsulated structures will be poorly represented. In literature we find a similar recommendation made by Gonzalez et al. [27] who discourages the use of plane-stress FEM to simulate encapsulated, meandered interconnects.

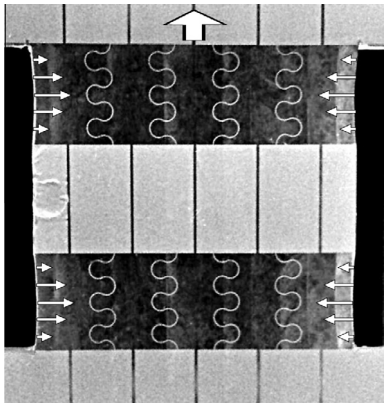

Fig. 13. Transverse deformation due to the Poisson effect at 10% tensile strain.

Finally, we have also been able to confirm the encapsulation thickness effect by comparing a half-encapsulated (t = 0.5 mm) reliability vehicle with one that was fully encapsulated (t = 1 mm). With encapsulation present on one side of the intercon-nect we have achieved a significant increase in the Weibull charac-teristic life under 10% extension fatigue test as shown in Fig. 9(b). Sweeping across smaller thickness was restricted by the manually handled, liquid injection molding procedure tolerance.

In Section 4.2.2 we show how the definition of the meandered interconnect encapsulation perimeter in the x–y plane affects the reliability. As a result of reducing the encapsulation size outside of the zone where metal is present we observe decreasing performance of the meanders closest to the PDMS boundary. This effect is again the result of the incompressibility of the PDMS encapsulation. Incompressibility results in transverse narrowing of the stretchable zone whenever tensile extension is exerted, as illustrated by a photograph in Fig. 13.

Because the outer tracks, number 1 and 4, are out of the "neutral axis" of the Poisson effect lateral compression they are subjected to lateral displacement field that adds to the deformation of the metal track due to the tensile force. As a result, diminished reliability is observed. Similar observation is made in [26] by FEM.

The practical implication of this result is, that, in order to maintain predictable and uniform failure distribution across a multiple-interconnect stretchable system, one should ensure that the meanders are placed about the center line of the Poisson compression in each interconnect and as far as possible from the encapsulation borders. For a large, grid-like system (Fig. 1(b)) this indicates the necessity for placing openings in the encapsulation to mechanically separate each stretchable interconnect from the other (demonstrator in Fig. 1(c) may serve as an example). Preferably, the interconnects should be running in pairs at most or otherwise have the outermost tracks far away from the encapsulation boundary (one could view the vehicle in Fig. 10(d) as a borderline case considering the presented material properties, geometry and test conditions). Ideally, one would want to be able to extrapolate the single interconnect geometry reliability testing result to reliability of a complete system consisting of k identical interconnects, using the size effect rule applied to Weibull distribution. By ensuring equivalence between meanders and stretchable interconnects in a large design this will be made possible. The benefit in that case is that the system failure CDF differs only by characteristic life compared to its single interconnect CDF [18]:

$$F(N) = 1 - \exp[-(N/\eta_k)^{\beta}] \text{ where } \eta_k = \frac{\eta}{k^{(1/\beta)}} \quad (1)$$

where η and β are single interconnect Weibull failure distribution estimates obtained in fatigue testing and k is the number of interconnects in the system.

In Section 4.2.3 no significant impact on reliability was found by encapsulating the meanders with materials ranging from Shore-A 29 to Shore-A 46 hardness. This result however, should be understood well in the context of the moderate strain test conditions (PDMS materials were far from entering increasing tangent modulus strain ranges) as well as the, effectively narrow, Young's modulus range covered. Following the study of [28] one could roughly translate the presented hardness range to 0.7–1.8 MPa range of Young Moduli (this conversion should not be treated formal as the hardness measurement was an apparent measure only). Together with limited amount of failure data the test has not enough power to yield significant differences. For higher tensile

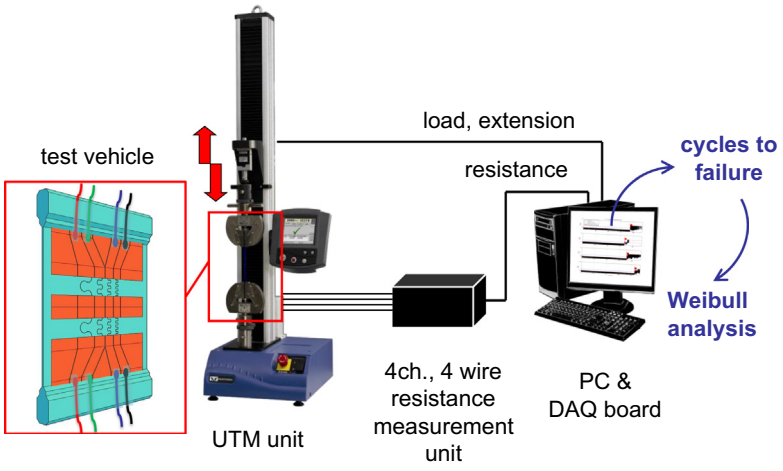

Fig. 14. The endurance test setup.

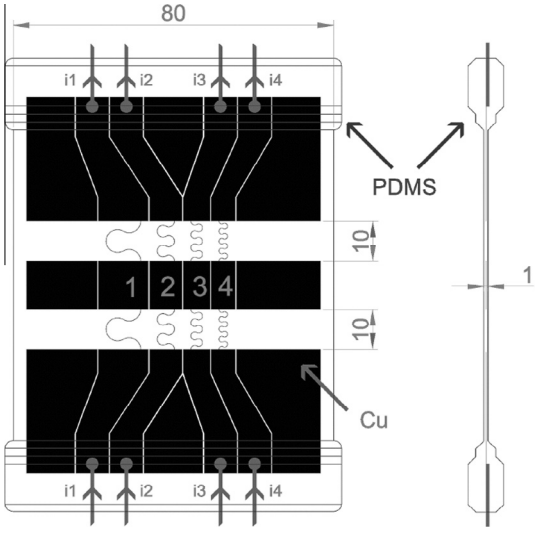

Fig. 15. Base test vehicle dimensions (mm).

extensions as well as wider Shore A range of materials one should expect detrimental impact of harder encapsulation on the reliability to be much more pronounced as suggested by earlier modeling studies [27]. For moderate interconnect strains (here 10% or less) the designers can freely choose encapsulation materials from the lower Shore A range (29–46 Shore A) based on other than cyclic reliability, application-specific criteria (e.g. optical properties).

6. Conclusions

We have presented a number of reliability and simulation studies where stretchable meandered interconnects were subjected to 10% repeated, uniaxial tensile extension while varying the interconnect geometry and encapsulation materials. We have identified a strong coupling between encapsulation thickness and meanders aspect ratio which indicate that already relatively thin (>500 μm) and soft encapsulation ($E = 0.7$ MPa), combined with large aspect ratio meanders ($R/W > 14$), produce extremely low reliabilities. We indicate that the use of small meanders ($R \leq 1$ mm) can be beneficial to create systems that run very low risk of failure during normal life by having a very well defined failure time (high Weibull β parameter). Reduction of encapsulation thickness is always to the benefit of interconnect fatigue life. Misalignment between meander direction and the tensile forces direction should be avoided or carefully monitored as possible source of early failures. Current results, as well as our previous findings, confirm that the transition zone to the flexible area is not improved by in-plane tapering of the meander ends in short interconnects. Provided that $R/W \leq 14$ a simple transition (FSTR0) is most optimal. A general recommendation is made to place meanders about the center of Poisson lateral compression in the encapsulation. This is necessary to maintain equal reliabilities of neighboring meanders. One way to translate this concept for a large stretchable system is to decouple neighboring bundles of interconnects by creating openings in the encapsulation. Finally, we show that PDMS encapsulation materials with hardness anywhere in the range between 29 and 46 Shore-A, make little difference to the interconnect reliabilities provided that interconnect extension is limited to 10%.

Acknowledgments

This work was conducted in frame of the FP7 European project PLACE-it (Grant Agreement 0248048) (urlhttp://www.place-it-project.eu), under the financial support from the European Commission and Ghent University PhD grants. We would also like to acknowledge the kind support of Dow Corning who provided all the encapsulation materials.

Appendix A. Test setup

Fig. 14.

Appendix B. Test vehicle parameters

Fig. 15.

References

[1] Jablonski M, Bossuyt F, Vanfleteren J, Vervust T, de Vries H. Reliability of a stretchable interconnect utilizing terminated, in-plane meandered copper conductor. Microelectron Reliab 2013;53(7):956–63.
[2] Vanfleteren J, Gonzalez M, Bossuyt F, Hsu YY, Vervust T, De Wolf I, et al. Printed circuit board technology inspired stretchable circuits. MRS Bulletin 2012;37(3):254–60.
[3] Chun KY, Oh Y, Rho J, Ahn JH, Kim YJ, Choi HR, et al. Highly conductive, printable and stretchable composite films of carbon nanotubes and silver. Nat Nanotechnol 2010;5(12):853–7.

[4] Kai L, Yinghui S, Peng L, Xiaoyang L, Shoushan F, Kaili J. Cross-stacked superaligned carbon nanotube films for transparent and stretchable conductors. Adv Funct Mater 2011;21(14):2721–8.
[5] Lin L, Liu SY, Fu SR, Zhang SM, Deng H, Fu Q. Fabrication of highly stretchable conductors via morphological control of carbon nanotube network. Small 2013;9(21):3620–9.
[6] Lipomi DJ, Vosgueritchian M, Tee BCK, Hellstrom SL, Lee JA, Fox CH, et al. Skin-like pressure and strain sensors based on transparent elastic films of carbon nanotubes. Nat Nanotechnol 2011;6(12):788–92.
[7] Sekitani T, Someya T. Stretchable, large-area organic electronics. Adv Mater 2010;22(20):2228–46.
[8] Wakuda D, Suganuma K. Stretchable fine fiber with high conductivity fabricated by injection forming. Appl Phys Lett 2011;98(7).
[9] Xu F, Wang X, Zhu YT, Zhu Y. Wavy ribbons of carbon nanotubes for stretchable conductors. Adv Funct Mater 2012;22(6):1279–83.
[10] Xu F, Zhu Y. Highly conductive and stretchable silver nanowire conductors. Adv Mater 2012;24(37):5117–22.
[11] Jahanshahi A, Salvo P, Vanfleteren J. Reliable stretchable gold interconnects in biocompatible elastomers. J Polym Sci Part B-Polym Phys 2012;50(11):773–6. 201.
[12] Jahanshahi A, Gonzalez M, van den Brand J, Bossuyt F, Vervust T, Verplancke R, et al. Stretchable circuits with horseshoe shaped conductors embedded in elastic polymers. Japanese J Appl Phys 2013;52(5).
[13] Loher T, Seckel M, Vieroth R, Dils C, Kallmayer C, Ostmann A, Aschenbrenner R, Reichl H, IEEE. Stretchable electronic systems: Realization and applications. 2009 11th Electronics packaging technology conference (Eptc 2009); 2009, p. 893–8.
[14] Sosin S, Zoumpoulidis T, Bartek M, Wang L, Dekker R, Jansen KMB, Ernst LJ. Free-standing, parylene-sealed copper interconnect for stretchable silicon electronics; 2008, p. 1339–45.
[15] Sosin S, Zoumpoulidis T, Bartek M, Wang L, Jansen KMB, Ernst LJ, IEEE. Mesh interconnects for silicone embedded stretchable silicon electronics. In: 10th Electronics packaging technology conference, electronics packaging technology conference proceedings; 2008, p. 230–5.
[16] Lacour SP, Jones J, Wagner S, Li T, Suo ZG. Stretchable interconnects for elastic electronic surfaces. Proc IEEE 2005;93(8):1459–67.
[17] Bossuyt F, Guenther J, Lher T, Seckel M, Sterken T, de Vries J. Cyclic endurance reliability of stretchable electronic substrates. Microelectron Reliab 2011;51(3):628–35.
[18] Nelson WB. Applied life data analysis. Willey; 2008.
[19] N.I. of Standards and Technology, NIST/sematech e-handbook of statistical methods.
[20] Myung IJ. Tutorial on maximum likelihood estimation. J Mathe Psychol 2003;47(1):90–100.
[21] Balakrishnan N, Kateri M. On the maximum likelihood estimation of parameters of weibull distribution based on complete and censored data. Stat Probab Lett 2008;78(17):2971–5.
[22] Genschel U, Meeker WQ. A comparison of maximum likelihood and median-rank regression for weibull estimation. Quality Eng 2010;22(4):236–55.
[23] Gonzalez M, Axisa F, Bossuyt F, Hsu YY, Vandevelde B, Vanfleteren J. Design and performance of metal conductors for stretchable electronic circuits. Circuit World 2009;35(1):22–9.
[24] Hsu Y-Y, Dimcic B, Gonzalez M, Bossuyt F, Vanfleteren J, De Wolf I. Reliability assessment of stretchable interconnects. In: Microsystems packaging assembly and circuits technology conference (IMPACT), 2010 5th International; Oct 2010, p. 1–4.
[25] Hsu YY, Gonzalez M, Bossuyt F, Axisa F, Vanfleteren J, De Wolf I. The effects of encapsulation on deformation behavior and failure mechanisms of stretchable interconnects. Thin Solid Films 2011;519(7):2225–34.
[26] Gonzalez M, Vandevelde B, Christiaens W, Hsu YY, Iker F, Bossuyt F, et al. Design and implementation of flexible and stretchable systems. Microelectron Reliab 2011;51(6):1069–76.
[27] Gonzalez M, Axisa F, Vanden Bulcke M, Brosteaux D, Vandevelde B, Vanfleteren J. Design of metal interconnects for stretchable electronic circuits using finite element analysis. EUROSIME 2007: Thermal, mechanical and multi-physics simulation and experiments in micro-electronics and micro-systems, proceedings; 2007, p. 110–5.
[28] Meththananda IM, Parker S, Patel MP, Braden M. The relationship between shore hardness of elastomeric dental materials and young's modulus. Dental Mater 2009;25(8):956–9.